



Proppant transport in hydraulic fracturing: Crack tip screen-out in KGD and P3D models



E.V. Dontsov, A.P. Peirce*

Department of Mathematics, University of British Columbia, Vancouver, BC, V6T 1Z2, Canada

ARTICLE INFO

Article history:

Received 20 August 2014

Received in revised form 19 February 2015

Available online 14 March 2015

Keywords:

Hydraulic fracturing

Proppant transport

Numerical modeling

ABSTRACT

The aim of this study is to develop a model for proppant transport in hydraulic fractures capable of capturing both gravitational settling and tip screen-out effects, while prohibiting the particles from reaching the crack tips by imposing a width restriction based on the particle size. First, the equations that govern the propagation of hydraulic fractures and the proppant transport inside them are formulated. They are based on the solution for the steady flow of a viscous fluid, mixed with spherical particles, in a channel, which is obtained assuming an empirical constitutive model. This proppant transport model is applied to two fracture geometries – Khristianovich–Zhel'tov–Geertsma–De Klerk (KGD) and pseudo-3D (P3D). Numerical simulations show that the proposed method makes it possible to capture proppant plug formation and growth, as well as the gravitational settling for both geometries. A dimensionless parameter, whose magnitude reflects the intensity of the settling, is introduced for the P3D fracture.

© 2015 Elsevier Ltd. All rights reserved.

1. Introduction

Hydraulic fracturing is a process whereby the fluid pressure due to fluid injection into a crack is the driving force for the fracture opening and propagation. Among the multiple uses of hydraulic fracturing, such as accelerating the waste remediation process (Frank and Barkley, 2005), waste disposal (Abou-Sayed et al., 1989), or preconditioning in rock mining (Jeffrey and Mills, 2000), oil and gas reservoir stimulation (Economides and Nolte, 2000) stands out as one of the most common applications. Recognizing the significance of hydraulic fracturing, many studies have been devoted to the modeling and numerical simulation of this phenomenon. Starting from the work of Khristianovich and Zhel'tov (1955), further examples of the analytical modeling can be found in Garagash and Detournay (2000), Adachi and Detournay (2002), Detournay and Garagash (2003) and Detournay (2004), where the near tip solutions and regimes of propagation are studied, while reviews of the existing numerical approaches aiming to predict hydraulic fracture propagation are given in Adachi et al. (2007) and Peirce and Detournay (2008).

The problem of hydraulic fracturing is challenging to analyze due to a variety of physical processes that are involved in the problem, such as fluid flow inside the fracture, fluid leak-off to

the surrounding rock, the rock fracturing due to crack propagation, and, in some cases, elastic interaction with natural fractures or other hydraulic fractures. Moreover, the fracturing fluid can be non-Newtonian, and its properties may vary with time and temperature. To effectively model the process, however, many assumptions are typically made. For instance, the fluid is assumed to be Newtonian, the flow is assumed to be laminar, the behavior of the rock is taken as linear elastic, poroelastic effects are typically neglected, the geometry of the fracture is greatly simplified to one-dimensional, radial, or planar etc. Even with these simplifications, the phenomenon of hydraulic fracturing is difficult to model, as it requires the solution of a nonlinear problem with a singularity, in which the nonlinearity comes from the lubrication equation and the singularity typically appears at the crack tip. This study aims to add an additional aspect to the problem, namely, the movement of proppant within the fracture. Typically, proppant is used to prevent the fracture from closing once the well is depressurized. In this case, modeling the fracture propagation driven only by a viscous fluid is not sufficient, since the proppant, blended with the fracturing fluid alters the properties of the fracturing fluid. Incorporating the effects associated with the presence of particles poses an additional challenging problem, which is addressed in this study. As mentioned in Adachi et al. (2007), in hydraulic fracturing problems, the slurry is typically modeled as a Newtonian fluid with the effective viscosity given by an empirical function of proppant content. In addition, a uniform particle distribution across the fracture is assumed and the slip velocity

* Corresponding author.

E-mail address: peirce@math.ubc.ca (A.P. Peirce).

only due to gravity is considered. In contrast, the current study utilizes an approach developed in [Dontsov and Peirce \(2014\)](#), where the governing equations for the slurry and the proppant transport are obtained based on the empirical constitutive model for the slurry introduced by [Boyer et al. \(2011\)](#). This model accounts for the non-uniform particle distribution across the channel, slip velocity induced by the slurry flow, and captures the transition from Poiseuille's flow for small particle concentrations to Darcy's law for nearly maximum proppant content.

It is also important to highlight a two phase model proposed by [Boronin and Osiptsov \(2010\)](#), and work by [Chekhonin and Levonyan \(2012\)](#), where proppant plug formation near the crack tip is studied. In the latter study, the one-dimensional problem of KGD fracture propagation is considered, and the problem is tackled using a double moving coordinate system. One coordinate is scaled by the length of the crack and another by the distance from the inlet to the proppant plug, in which case the boundaries of the plug are tracked automatically based on the calculated distances. While this approach works well for a 1D geometry, its generalization to 2D fractures seems to be tremendously difficult since two moving boundaries cannot easily be resolved using scaling. Some of the studies, however, investigate just the flow of the slurry, i.e. the mixture of fluid with the particles, and do not apply it to the fracture propagation problem. One example is a study by [Eskin and Miller \(2008\)](#), in which the granular temperature is used to account for micro-level particle movements. To address the problem, this study aims to develop a model for hydraulic fracturing by a slurry, which accounts for the mechanics of the slurry, while, at the same time, is sufficiently simple that it can be implemented into a hydraulic fracturing simulator.

The paper is organized as follows. First, the governing equations for the slurry flow and proppant transport inside hydraulic fractures, obtained in [Dontsov and Peirce \(2014\)](#), are summarized in Section 2. Then, in Sections 3 and 4, the governing equations for the slurry and proppant transport are embedded into the fracture propagation problems (respectively KGD and P3D) and the complete problems are solved numerically.

2. Background

This section aims to summarize background information that is necessary to develop a computational scheme for proppant transport inside hydraulic fractures. The approach is based on the slurry flow solution in the channel, developed in [Dontsov and Peirce \(2014\)](#). This solution is, in turn, based on the empirical constitutive model for the mixture of a Newtonian fluid and spherical particles introduced in [Boyer et al. \(2011\)](#). [Fig. 1](#) shows the schematics of the fracture and the associated coordinate system, where x is the coordinate along the fracture in the horizontal direction, z is the vertical axis (it is assumed that the fracture is contained in a vertical plane), while y is the coordinate across the fracture. As shown in

[Dontsov and Peirce \(2014\)](#), the balance equations for the slurry and proppant can be written as

$$\begin{aligned} \frac{\partial w}{\partial t} + \nabla \cdot \mathbf{q}^s + g_L &= 0, \\ \frac{\partial w \bar{\phi}}{\partial t} + \nabla \cdot \mathbf{q}^p &= 0, \end{aligned} \quad (1)$$

where w is the width of the fracture, $\bar{\phi} = \langle \phi \rangle / \phi_m$ is the normalized proppant concentration averaged over fracture the width, i.e. in the y direction, $\phi_m = 0.585$ is the maximum allowed proppant concentration, g_L represents leak-off, while \mathbf{q}^s and \mathbf{q}^p denote respectively the slurry and proppant fluxes. Note that the fluxes have two components, namely x and z , and consequently, $\nabla = (\partial/\partial x, \partial/\partial z)$ in (1). The expressions for the fluxes are

$$\begin{aligned} \mathbf{q}^s &= -\frac{w^3}{12\mu^f} \hat{Q}^s \left(\bar{\phi}, \frac{w}{a} \right) \nabla \hat{p}, \\ \mathbf{q}^p &= B \left(\frac{w}{a} \right) \hat{Q}^p \left(\bar{\phi}, \frac{w}{a} \right) \mathbf{q}^s - B \left(\frac{w}{a} \right) \frac{a^2 w}{12\mu^f} (\rho^p - \rho^f) g \mathbf{e}_z \hat{G}^p \left(\bar{\phi}, \frac{w}{a} \right), \end{aligned} \quad (2)$$

where μ^f is the clear fluid viscosity, \hat{p} is the fluid pressure corrected by hydrostatic pressure, $\rho^p - \rho^f$ is the difference between proppant and fluid mass densities, g is the gravitational acceleration, a is the particle radius, B is a, so-called, blocking function, while the functions \hat{Q}^s , \hat{Q}^p and \hat{G}^p come from the slurry flow solution ([Dontsov and Peirce, 2014](#)).

The blocking function B is introduced to capture proppant bridging that occurs when the fracture width is on the order of several particle diameters. For the purpose of calculations, the blocking function is taken as

$$\begin{aligned} B \left(\frac{w}{a} \right) &= \frac{1}{2} H \left(\frac{w}{2a} - N \right) H \left(\frac{w_B - w}{2a} \right) \left[1 + \cos \left(\pi \frac{w_B - w}{2a} \right) \right] \\ &\quad + H \left(\frac{w - w_B}{2a} \right), \end{aligned} \quad (3)$$

where N represents "several" particle diameters, H denotes the Heaviside step function, while $w_B = 2a(N + 1)$, which provides a continuous vanishing of the function and helps in the numerical implementation. $N = 3$ is chosen for all examples considered in this paper.

Functions \hat{Q}^s , \hat{Q}^p and \hat{G}^p can be expressed in a simpler form as

$$\begin{aligned} \hat{Q}^s \left(\bar{\phi}, \frac{w}{a} \right) &= Q^s(\bar{\phi}) + \frac{a^2}{w^2} \bar{\phi} D, \\ \hat{Q}^p \left(\bar{\phi}, \frac{w}{a} \right) &= \frac{w^2 Q^p(\bar{\phi})}{w^2 Q^s(\bar{\phi}) + a^2 \bar{\phi} D}, \\ \hat{G}^p \left(\bar{\phi}, \frac{w}{a} \right) &= G^p(\bar{\phi}) - \frac{w^2 G^s(\bar{\phi}) Q^p(\bar{\phi})}{w^2 Q^s(\bar{\phi}) + a^2 \bar{\phi} D}, \end{aligned} \quad (4)$$

where Q^s , Q^p , G^s and G^p are functions of $\bar{\phi}$ only and are calculated numerically, $D = 8(1 - \phi_m)^{\bar{\alpha}} / 3\phi_m$ is related to the permeability of the packed particles, $\bar{\alpha} = 4.1$, see [Dontsov and Peirce \(2014\)](#). As

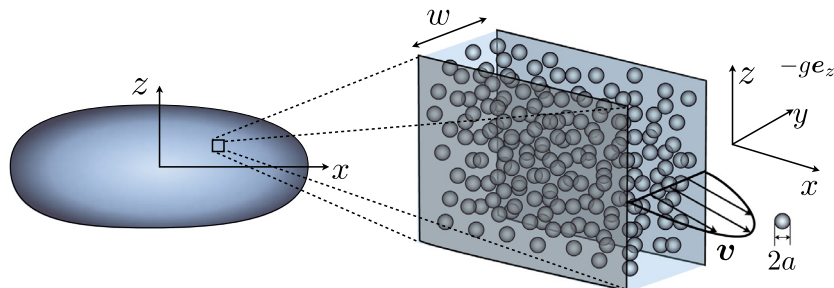


Fig. 1. Schematics of the hydraulic fracture (left) and the slurry flow inside it (right).

an illustration, Fig. 2 plots the functions \hat{Q}^s , \hat{Q}^p and \hat{G}^p versus normalized proppant concentration $\bar{\phi}$ for different values of the parameter w/a . Function \hat{Q}^s represents the reciprocal of the effective slurry velocity, while the term with D in \hat{Q}^s accounts for a Darcy's law. So, the slurry flux in (2) is able to capture the transition from Poiseuille's flow (with effective viscosity) to Darcy's filtration flow as the concentration reaches nearly the maximum value. The function \hat{Q}^p in the proppant flux in (2) describes the proppant motion caused by the slurry flow, while \hat{G}^p captures gravitational settling of the particles.

It is the difference between the fluid pressure and hydrostatic pressure, denoted by \hat{p} , that drives the slurry, see (2). According to Dontsov and Peirce (2014), \hat{p} is given by

$$\hat{p} = p - p_h = p + \rho^f g z + (\rho^p - \rho^f) g \phi_m \bar{\phi} z + (\rho^p - \rho^f) g \int_0^z \frac{a^2 G^s(\bar{\phi})}{w^2 Q^s(\bar{\phi}) + a^2 \bar{\phi} D} dz, \tag{5}$$

where p is the fluid pressure and p_h is the hydrostatic pressure. The hydrostatic pressure is the driving force for buoyancy-driven fractures (Lister, 1990), which is typically neglected for other hydraulic fracturing problems for simplicity. For this reason, all calculations in this paper neglect the hydrostatic pressure, which effectively replaces \hat{p} by the fluid pressure p in (2).

It is important to outline the assumptions of the proppant transport model that is adopted in this study. Firstly, since a continuum approach is used, the model is only applicable in regions where the fracture width exceeds several particle diameters. Clearly, this condition is violated near the fracture tip, where proppant size becomes comparable to the fracture width and bridging occurs. At the same time, the model is applicable in regions that are away from the fracture tip. Secondly, it is assumed that all particles are spherical and have the same diameter. To incorporate effects associated with non-spherical particles, a new constitutive model for the flow of such particles would have to be developed first. Thirdly, the steady state slurry flow is used to formulate the model. Hence, the regions of a fracture where slurry flow changes rapidly are not described accurately. For instance, if a clear fluid is followed by a slurry with a finite proppant concentration, the evolution of the proppant front will entail rapid flow fluctuations, which leads to inaccurate predictions near the clear fluid/slurry boundary.

3. Numerical solution for a KGD fracture

3.1. Problem formulation

To better understand the effects associated with the presence of particles (or proppant) on hydraulic fracture propagation, it is instructive to consider the simplest one-dimensional case of a KGD fracture in the presence of stress barriers. To this end it is

assumed that the fracture lies along z axis and occupies interval $(-l_1, l_2)$ (see Fig. 3), where l_1 and l_2 are the extensions of the fracture respectively in the negative and positive z directions. By using Carter's leak-off model (Carter, 1957) and adding the source terms, the governing equations for fluid flow within the fracture including proppant can be deduced from (1) as

$$\begin{aligned} \frac{\partial w}{\partial t} + \frac{\partial q_z^s}{\partial z} + \frac{C'}{\sqrt{t - t_0(z)}} &= Q_0 \delta(z), \\ \frac{\partial w \bar{\phi}}{\partial t} + \frac{\partial q_z^p}{\partial z} &= \bar{\phi}_0 Q_0 \delta(z), \end{aligned} \tag{6}$$

where $-l_1 \leq z \leq l_2$, and

$$\begin{aligned} q_z^s &= -\frac{w^3}{\mu'} \hat{Q}^s(\bar{\phi}) \frac{\partial p}{\partial z}, \\ q_z^p &= B \left(\frac{w}{a} \right) \hat{Q}^p \left(\bar{\phi}, \frac{w}{a} \right) q_z^s - B \left(\frac{w}{a} \right) \frac{a^2 w}{\mu'} (\rho^p - \rho^f) g \hat{G}^p \left(\bar{\phi}, \frac{w}{a} \right). \end{aligned} \tag{7}$$

Here $\mu' = 12\mu^f$ is the scaled viscosity, $C' = 2C_L(C_L - \text{Carter's leak-off coefficient})$, Q_0 is the injection volume of the slurry per unit time, while $\bar{\phi}_0$ is the normalized volume fraction of proppant at the source. To close the system of Eqs. (6), one needs to add the elasticity equation (see e.g. Adachi, 2001), which can be written as

$$p - \Delta \sigma(z) = -\frac{E'}{4\pi} \int_{-l_1}^{l_2} \frac{w ds}{(s - z)^2}, \tag{8}$$

where $E' = E/(1 - \nu^2)$ is the plane-strain Young's modulus, the integral is understood in the sense of a Hadamard finite part, while $\Delta \sigma(z)$ is an additional confining stress coming from the stress barriers. The boundary and propagation conditions at the tips are

$$\begin{aligned} q_z^s|_{z=-l_1} &= 0, & q_z^p|_{z=-l_1} &= 0, & w &\rightarrow \frac{K'}{E'}(z + l_1)^{1/2}, & z &\rightarrow -l_1, \\ q_z^s|_{z=l_2} &= 0, & q_z^p|_{z=l_2} &= 0, & w &\rightarrow \frac{K'}{E'}(l_2 - z)^{1/2}, & z &\rightarrow l_2, \end{aligned} \tag{9}$$

where $K' = 8K_{Ic}/\sqrt{2\pi}$ is the scaled fracture toughness.

3.2. Numerical algorithm

The problem under consideration is split into two steps: (i) solve for the propagation of the fracture, i.e. coupling (6a), (8) and (9) and (ii) solve for the proppant transport, i.e. (6b) with the boundary conditions given in (9). In other words, at each time step, first (6a), (8) and (9) are solved to update the fracture width profile and length, and then (6b) is solved to find the new proppant concentration distribution over the fracture length. This subsection is aimed to cover both steps in the procedure.

To facilitate the numerical solution of the moving-boundary problem under consideration, a double moving mesh is introduced. In this case, negative and positive components of the x coordinate are normalized respectively by l_1 and l_2 , so that

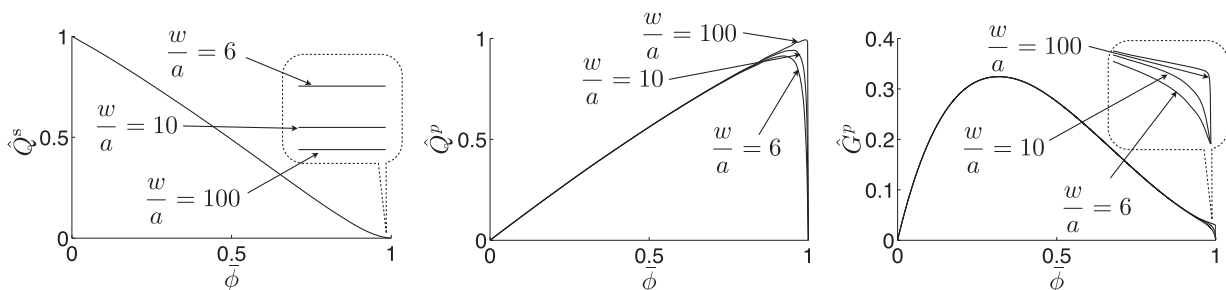


Fig. 2. Variation of the functions \hat{Q}^s , \hat{Q}^p and \hat{G}^p versus normalized proppant concentration $\bar{\phi}$ for different values of the parameter w/a .

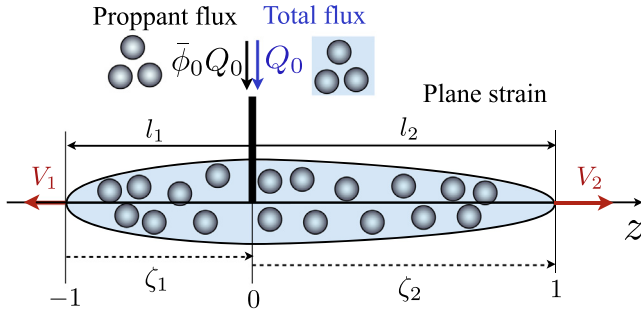


Fig. 3. Schematics of asymmetric KGD fracture.

$$\zeta_1 = \frac{z}{l_1}, \quad -1 \leq \zeta_1 \leq 0, \quad \zeta_2 = \frac{z}{l_2}, \quad 0 \leq \zeta_2 \leq 1, \quad (10)$$

and

$$\begin{aligned} \frac{\partial(\cdot)}{\partial t} \Big|_z &= \frac{\partial(\cdot)}{\partial t} \Big|_{\zeta_1} - \frac{V_1 \zeta_1}{l_1} \frac{\partial(\cdot)}{\partial \zeta_1} \Big|_{\zeta_1}, & \frac{\partial(\cdot)}{\partial z} \Big|_z &= \frac{1}{l_1} \frac{\partial(\cdot)}{\partial \zeta_1} \Big|_{\zeta_1}, & z \leq 0, \\ \frac{\partial(\cdot)}{\partial t} \Big|_z &= \frac{\partial(\cdot)}{\partial t} \Big|_{\zeta_2} - \frac{V_2 \zeta_2}{l_2} \frac{\partial(\cdot)}{\partial \zeta_2} \Big|_{\zeta_2}, & \frac{\partial(\cdot)}{\partial z} \Big|_z &= \frac{1}{l_2} \frac{\partial(\cdot)}{\partial \zeta_2} \Big|_{\zeta_2}, & z \geq 0, \end{aligned} \quad (11)$$

where $V_1 = dl_1/dt$ and $V_2 = dl_2/dt$ are the velocities of crack propagation in the negative and positive z directions, as indicated in the Fig. 3. By substituting (11) into (6), one can write

$$\begin{aligned} \frac{\partial w}{\partial t} - \frac{V_{1,2}}{l_{1,2}} \zeta_{1,2} \frac{\partial w}{\partial \zeta_{1,2}} + \frac{1}{l_{1,2}} \frac{\partial q_z^s}{\partial \zeta_{1,2}} + \frac{C'}{\sqrt{t-t_0}(l_{1,2}\zeta_{1,2})} &= \frac{Q_0}{l_{1,2}} \delta(\zeta_{1,2}), \\ \frac{\partial w \bar{\phi}}{\partial t} + \frac{V_{1,2}}{l_{1,2}} w \bar{\phi} + \frac{1}{l_{1,2}} \frac{\partial \tilde{q}_z^p}{\partial \zeta_{1,2}} &= \frac{\bar{\phi}_0 Q_0}{l_{1,2}} \delta(\zeta_{1,2}), \end{aligned} \quad (12)$$

where

$$\tilde{q}_z^p = q_z^p - V_{1,2} \zeta_{1,2} w \bar{\phi},$$

and the indices 1, 2 correspond respectively to the regions $z \leq 0$ and $z \geq 0$ (see (11)).

Fracture propagation. To formulate the numerical scheme, first, the width is approximated by a piecewise constant function in the ζ_1 and ζ_2 domains. In this case, the elasticity Eq. (8) can be discretized in obtain

$$\mathbf{p}^j = \mathbf{C}^i \mathbf{w}^i + \mathbf{p}_{\text{tip}}^i + \Delta \boldsymbol{\sigma}^i, \quad (13)$$

where \mathbf{p}^j and \mathbf{w}^i denote respectively pressure and width vectors (defined at all grid points and time t_i), $\mathbf{p}_{\text{tip}}^i$ is the pressure correction at the tip (defined only at the tip points and time t_i),

$$\begin{aligned} (\mathbf{C}^i)_{jk} &= -\frac{E' l_1 \Delta \zeta}{4\pi} \left((z_j - z_k)^2 - \frac{1}{4} l_1^2 \Delta \zeta^2 \right)^{-1}, & z_k < 0, \\ (\mathbf{C}^i)_{jk} &= -\frac{E' (l_1 + l_2) \Delta \zeta}{8\pi} \left(\left(z_j - \frac{1}{2} l_2 \Delta \zeta \right) \left(z_j + \frac{1}{2} l_1 \Delta \zeta \right) \right)^{-1}, & z_k = 0, \\ (\mathbf{C}^i)_{jk} &= -\frac{E' l_2 \Delta \zeta}{4\pi} \left((z_j - z_k)^2 - \frac{1}{4} l_2^2 \Delta \zeta^2 \right)^{-1}, & z_k > 0 \end{aligned}$$

is the elasticity matrix (depends on time through l_1 and l_2), while $\Delta \boldsymbol{\sigma}^i$ is the term that comes from the presence of stress barriers (again, this depends on time through l_1 and l_2). Here $\Delta \zeta$ denotes the mesh size associated with the discretized coordinates ζ_1 and ζ_2 (the same element size is used for both ζ_1 and ζ_2), while z_j refers to the location of the j th element of \mathbf{w}^i . The tip pressure is added as an unknown since the accuracy of the pressure at the tip is poor due to the singular nature of the kernel in (8). By using the backward Euler scheme to approximate the time derivative, Eqs. (12a) and (13) can be written in a discretized form as

$$\frac{\mathbf{w}^i - \mathbf{w}^{i-1}}{t_i - t_{i-1}} - \mathbf{B}^i \mathbf{w}^i + \mathbf{A}(\mathbf{w}^i, \bar{\phi}^i) \mathbf{C}^i \mathbf{w}^i + \mathbf{A}(\mathbf{w}^i, \bar{\phi}^i) (\mathbf{p}_{\text{tip}}^i + \Delta \boldsymbol{\sigma}^i) = \mathbf{S}^{i-1/2}, \quad (14)$$

where \mathbf{B}^i is the matrix that accounts for the “moving mesh terms” coming from the time derivatives in (11), $\mathbf{A}(\mathbf{w}^i, \bar{\phi}^i)$ approximates the flux divergence term, while $\mathbf{S}^{i-1/2}$ accounts for the source and leak-off terms. Central differences are used to calculate matrix \mathbf{B}^i , while $\mathbf{A}(\mathbf{w}^i, \bar{\phi}^i)$ is calculated using

$$\frac{1}{l_{1,2}} \left(\frac{\partial q_z^s}{\partial \zeta} \right)_j^i = J_{J+1/2}^A \frac{p_{j+1}^i - p_j^i}{(l_{1,2} \Delta \zeta)^2} - J_{J-1/2}^A \frac{p_j^i - p_{j-1}^i}{(l_{1,2} \Delta \zeta)^2} = A_{jm} p_m^i, \quad (15)$$

where

$$J_{J\pm 1/2}^A = -\frac{w_{j\pm 1/2}^i}{l_{1,2}} \left((w_{j\pm 1/2}^i)^2 Q^s(\bar{\phi}_{j\pm 1/2}^i) + a^2 \bar{\phi}_{j\pm 1/2}^i D \right),$$

and $w_{j\pm 1/2}^i = \frac{1}{2} (w_{j+1}^i + w_j^i)$, while $\bar{\phi}_{j\pm 1/2}^i$ are defined at the midpoints, see Fig. 4. Note that the pressure is defined at the same points as the width, while coefficients $J_{j\pm 1/2}^A$ share the mesh with $\bar{\phi}_{j\pm 1/2}^i$. The discretized Eq. (14) approximates the corresponding differential equation inside the domain, and thus does not capture the boundary conditions. To find the discretized equations for the boundary nodes, one needs to integrate Eq. (6a) over the tip elements and use the boundary conditions (9). This provides two equations, which can be written in the general form as

$$\mathbf{p}_{\text{tip}}^i = \mathbf{p}_{\text{tip}}^i(V_1, V_2, \mathbf{w}^i, \bar{\phi}^i). \quad (16)$$

If the correction for the tip were not necessary, then (16) would allow us to find the unknown tip velocities V_1 and V_2 and close the system of Eqs. (14). However, since the pressure at the tip elements cannot be computed accurately, one has to impose two additional conditions. One possibility is to assume that the width in the tip elements should follow the appropriate asymptotic solution, as used in Peirce and Detournay (2008), and use the corresponding asymptotic formulas for the tip velocity. In this case, two additional equations are

$$V_1 = \bar{V}_1(\mathbf{w}^i, C', K'), \quad V_2 = \bar{V}_2(\mathbf{w}^i, C', K'), \quad (17)$$

where functions \bar{V}_1 and \bar{V}_2 depend on the regime of propagation of the hydraulic fracture. Note that the proppant cannot occupy the near-tip elements due to the “blocking” functions, introduced in (3), for this reason, “classical” asymptotic solutions can be used. For instance, in the viscous regime, i.e. in situation when $C' = K' = 0$, one has

$$V_1 = \frac{(w_2^i)^3}{\beta_m^3 (l_1 \Delta \zeta)^2}, \quad V_2 = \frac{(w_{N_c-1}^i)^3}{\beta_m^3 (l_2 \Delta \zeta)^2} \quad (18)$$

where $\beta_m = 2^{1/3} \cdot 3^{5/6}$, while w_2^i and $w_{N_c-1}^i$ are the values of the width for the second and the penultimate nodes. Note that $w_1^i = w_{N_c}^i = 0$ due to the boundary conditions in (9). More information about asymptotic solutions for the KGD fracture can be found in Adachi (2001).

Finally, at each time step, Eqs. (14) and (16) are solved iteratively using the appropriate expression for the tip velocities (17). Then, the fracture footprint is updated using

$$l_j^i = l_j^{i-1} + (t_i - t_{i-1}) V_j, \quad j = 1, 2.$$

Proppant transport. As indicated earlier in this section, first, the fracture propagation is determined for a given time step, and then (12b) is solved numerically to update the particle distribution over the fracture length. Eq. (12b) has the form of a conservation law,

which is both nonlinear and heterogeneous. To deal with such a problem, a finite volume method with *cell-centered flux functions* (Bale et al., 2002) is used. In particular, the moving mesh term is integrated by parts, and (12b) is discretized as follows

$$\frac{(\mathbf{w}\bar{\phi})^i - (\mathbf{w}\bar{\phi})^{i-1}}{t_i - t_{i-1}} + \frac{V_{1,2}}{l_{1,2}}(\mathbf{w}\bar{\phi})^{i-1} + \mathbf{D}\mathbf{E}_{\pm 1/2}\bar{q}_z^{i-1} = \mathbf{S}_p^{i-1/2}, \quad (19)$$

where $\mathbf{S}_p^{i-1/2}$ is the source term, matrix \mathbf{D} is a finite difference operator, which employs a central difference scheme to approximate the flux derivative. i.e. $(\mathbf{D}\mathbf{A})_{j-1/2} = A_j^{i-1} - A_{j-1}^{i-1}$, $\mathbf{E}_{\pm 1/2}$ is a shift operator, which shifts the flux function evaluation either to the left or to the right by a half grid cell size, i.e. $\mathbf{E}_{\pm 1/2}A_j = A_{j\pm 1/2}$. Note that $(\mathbf{w}\bar{\phi})^i$ are defined at the grid points that correspond to $\bar{\phi}_{j\pm 1/2}^i$ (see Fig. 4), so that $(\mathbf{w}\bar{\phi})_{j\pm 1/2}^i = \frac{1}{2}(w_j^i + w_{j\pm 1}^i)\bar{\phi}_{j\pm 1/2}^i$. The most difficult challenge in using (19) is to determine how to use the shift operator appropriately to have a stable scheme.

An in-depth analysis of the nonlinear conservation laws (and the associated numerical schemes) entails finding the characteristics, which depend on the derivative of the nonlinear flux, i.e. $\partial\bar{q}_z^p/\partial(\mathbf{w}\bar{\phi})$ (see e.g. Bale et al., 2002; LeVeque, 2002). Unfortunately, the proppant flux \bar{q}_z^p depends on w , which, in turn, is functionally dependent upon $\bar{\phi}$ through (6a), so that exact evaluation of this derivative is not trivial. For this reason, it is assumed that the variation of w with respect $\bar{\phi}$ is small ($\partial w/\partial\bar{\phi} \approx 0$), in which case the differentiation of (6a) with respect to $\bar{\phi}$ yields:

$$q_z^s = \text{const.} \Rightarrow v_z^s = \frac{q_z^s}{w} = \text{const.}, \quad (20)$$

where v_z^s is an average velocity of the slurry, and “const.” means constant with respect to $\bar{\phi}$. The implication of Eq. (20) is that the velocity of the slurry may be taken as constant during the evaluation of the derivative of the flux, i.e.

$$\frac{\partial\bar{q}_z^p}{\partial(\mathbf{w}\bar{\phi})} = B\left(\frac{w}{a}\right)wv_z^s\frac{\partial}{\partial(\mathbf{w}\bar{\phi})}\left[\hat{Q}^p\left(\frac{w\bar{\phi}}{w}, \frac{w}{a}\right)\right] - B\left(\frac{w}{a}\right)\frac{a^2w}{\mu'}(\rho^p - \rho^f)g\frac{\partial}{\partial(\mathbf{w}\bar{\phi})}\left[\hat{G}^p\left(\frac{w\bar{\phi}}{w}, \frac{w}{a}\right)\right] - \frac{V_{1,2}}{l_{1,2}}\zeta_{1,2}. \quad (21)$$

One may also interpret the assumption $\partial w/\partial\bar{\phi} \approx 0$ and consequently (20) in a different way. In the numerical scheme, first the width profile is updated, and then the equation for particle concentration is solved. Once the width is calculated, it cannot be changed while solving the proppant transport equation (within the same time step), hence $w = \text{const.}$, which consequently implies (20). It is interesting to observe that according to Fig. 2, derivatives of the functions \hat{Q}^p and \hat{G}^p appearing in (21) can be large in magnitude for $\bar{\phi} \approx 1$. In particular, it can be shown that their absolute values behave like $w^2/a^2 \gg 1$. Note, however, that $\hat{Q}^s = O(a^2/w^2)$ and consequently $v_z^s = O(a^2/w^2)$ for such particle concentrations, so that the product of the derivative of \hat{Q}^p and v_z^s is $O(1)$ in terms of the small parameter a/w . Since a^2 multiplies the gravitational settling term in (21), the fact that the derivative of \hat{G}^p is $O(w^2/a^2)$ similarly does not make the whole term large in magnitude. This shows that even in the limit of very small particles, the flux derivative (21) is bounded. The width of the fracture can also be small, but, clearly, the differentiation in (21) cancels w and leads to some finite value of the flux derivative for small w .

Since (12b) has the form of a conservation law, Eq. (21) allows us to calculate the velocity of the nonlinear wave, which is then used to find the sign of the “wind” and utilize it in the numerical scheme. One of the best options is to use the Godunov scheme, which, however, requires the solution of the Riemann problem

(LeVeque, 2002). Unfortunately, finding the solution of the Riemann problem may be challenging and requires a significant amount of the computation time (since the proppant flux depends on functions that are computed numerically), for this reason an approximate Riemann solver is used. To assist with the construction of the numerical scheme, it is noted that $\bar{q}_z^p = \bar{q}_z^p(\mathbf{w}\bar{\phi}, w)$, and that the shock velocities between the elements can be defined as

$$V_j^{\text{sh}} = \frac{\bar{q}_z^p(w_{j+1/2}^i\bar{\phi}_{j+1/2}^i, w_{j+1/2}^i) - \bar{q}_z^p(w_{j-1/2}^i\bar{\phi}_{j-1/2}^i, w_{j-1/2}^i)}{w_{j+1/2}^i\bar{\phi}_{j+1/2}^i - w_{j-1/2}^i\bar{\phi}_{j-1/2}^i}, \quad (22)$$

where $w_{j\pm 1/2}^i = \frac{1}{2}(w_j^i + w_{j\pm 1}^i)$. Fig. 5 shows the algorithm for determining the proppant flux based on the sign of the “wind” (21) and the shock velocity (22). There are three cases, where: (a) the “wind”, calculated according to (21), is positive for both neighboring points, (b) the “wind” is negative for both neighboring points, and (c) the direction of the “wind” is different for the neighboring points. In the latter case, the shock velocity in (22) is used to determine the value of the proppant flux, see Fig. 5.

Since Eq. (19) represents an explicit scheme, stability poses a restriction on the magnitude of the time step $t_i - t_{i-1}$. In other words, the time step has to be reduced to make sure that the Courant–Friedrichs–Lewy (CFL) condition (LeVeque, 2002) is satisfied. On the other hand, since the numerical scheme for the crack opening (14) is implicit, there is no restriction on the time step for solving (14). To allow for arbitrary large time steps $t_i - t_{i-1}$ for the whole numerical algorithm, the time step $t_i - t_{i-1}$ is subdivided into small time steps when solving (19), each of which satisfies the CFL condition. This decomposition enables us to use large time steps for the stiff part of the problem (6a) and (8), which would require a time step restriction $\Delta t \sim O(\Delta z^3)$, while the less stiff Eq. (6b) can be treated explicitly as it only involves a CFL condition $\Delta t \sim O(\Delta z)$.

It should also be noted that the equations are first scaled and then solved numerically. Once the solution is obtained, the dimensions of the parameters are then recovered. More information about scaling for the KGD fracture can be found in Adachi (2001).

3.3. Numerical examples

This section is devoted to numerical examples that highlight the effects produced by the proppant. Due to the considerable number of parameters that influence the result, it is instructive to specify a reference set of parameters, and then change just some of them if needed. All numerical simulations in this section start at $t_{\text{start}} = 1$ s, assume a symmetric crack of length $l_1 = l_2 = 1$ m, and take the opening to be elliptic with the maximum width $w_{\text{max}} = 5 \times 10^{-4}$ m. The fracture is then propagated until $t_{\text{pr}} = 1000$ s using pure fluid, and thereafter the proppant is introduced, so for $t > t_{\text{pr}}$, the mixture of the proppant and the fluid is used. The simulations run until t_{end} , which is specified uniquely for each calculation. The input volume concentration of particles is taken $\bar{\phi}_0 = 0.2$, but note that $\bar{\phi}_0$ is the scaled concentration, so that the true concentration is $\phi_m\bar{\phi}_0$. Other parameters used for the calculations are $E' = 25 \times 10^9$ Pa for the plane strain modulus, $\mu' = 1.2$ Pa s for the viscosity (times 12), $Q_0 = 2 \times 10^{-4}$ m²/s for the inlet flux, $C' = 5 \times 10^{-5}$ m/s^{1/2} for the leak-off coefficient, $K_{1c} = 10^6$ Pa m^{1/2} for the fracture toughness, $a = 4 \times 10^{-4}$ m for the particle radius, $\Delta\rho = 1300$ kg/m³ for the difference in mass densities between the proppant and the fluid and $g = 9.8$ m/s² for the gravitational acceleration. A stress barrier is assumed to be symmetric, located $l_\sigma = 10$ m from the inlet, and to have a magnitude $\Delta\sigma = 2.5 \times 10^6$ Pa.

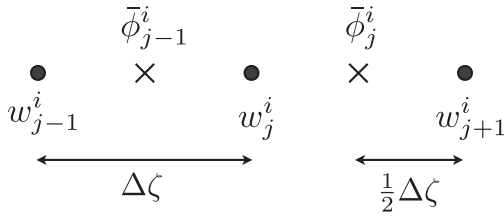


Fig. 4. Discretization of the width w and normalized particle concentration $\bar{\phi}$.

The problem with no leak-off is considered first. Fig. 6 plots pictures of the fracture width and proppant concentration at different time instants, as well as pressure and length histories. First of all, without the leak-off, the proppant does not accumulate rapidly in the tip regions, while, at the same time it can reach the bottom tip due to the gravitational settling. Even though the proppant changes the viscosity notably, its uneven distribution does not influence the symmetry much. This is because high viscosity has the most influence in the regions with high pressure gradients, i.e. near fracture tips. So, there is almost no influence of proppant

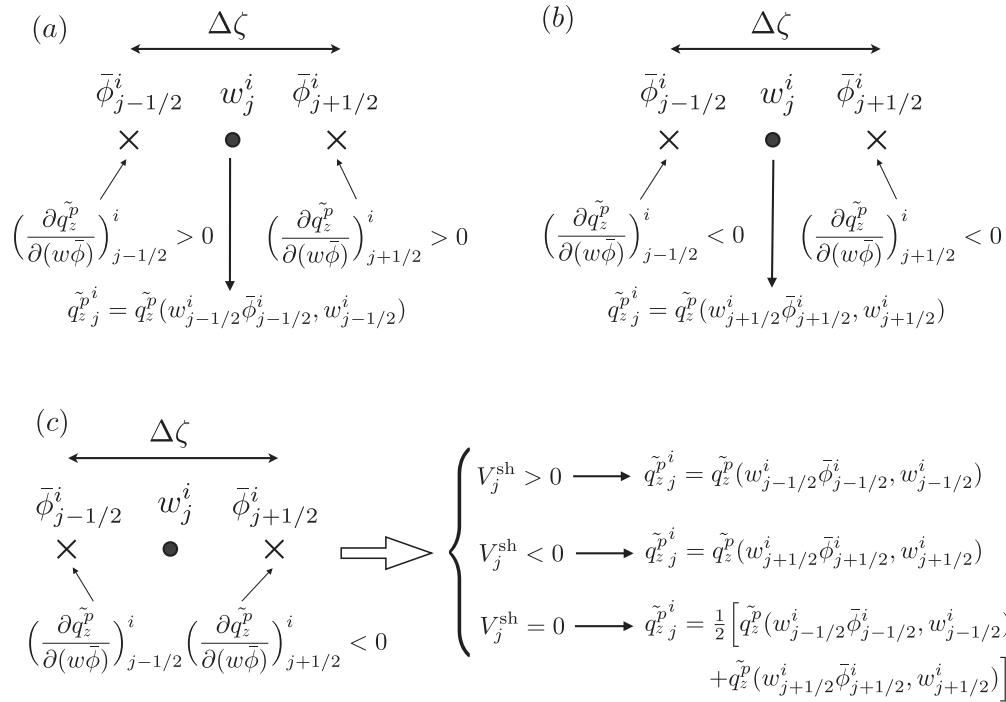


Fig. 5. Schematics of the algorithm for approximating the proppant flux at the point that corresponds to w_j^i : (a) if the “wind” at both neighboring points is positive, then use the “left” value, (b) if the “wind” at both neighboring points is negative, then use the “right” value, and (c) if the direction of the “wind” is different for neighboring points, then use the sign of V_j^{sh} to determine value of the flux.

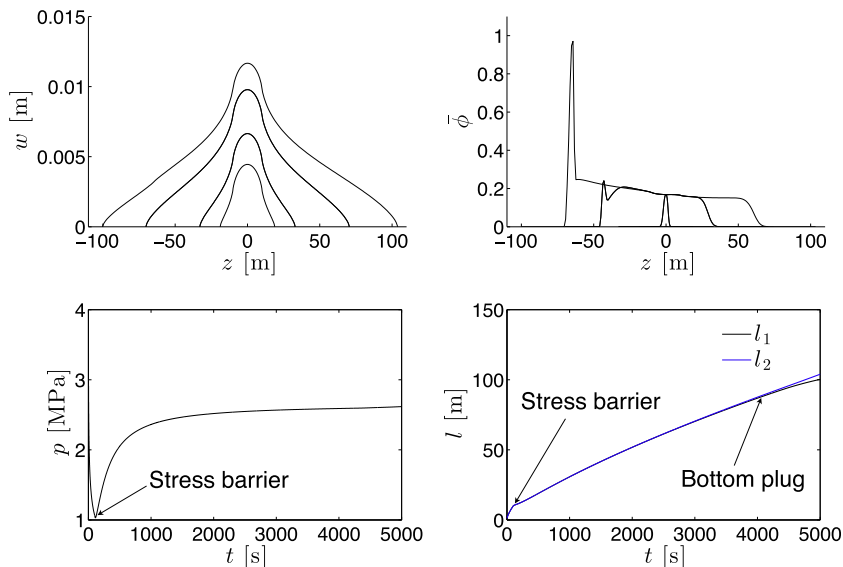


Fig. 6. The fracture width and proppant distribution (top pictures) for the reference parameter set and leak-off at different time instants $t_{\text{ev}} = 500$ s (no proppant at this time), 1100 s, 3000 s, and 5000 s. Bottom pictures show the histories of pressure at the inlet and the lengths l_1 (distance from the inlet to the bottom tip) and l_2 (distance from the inlet to the top tip).

before it reaches the tip region and starts to accumulate there. This hypothesis is supported by the length histories shown in Fig. 6. Indeed, noticeable asymmetry is induced only at $t \approx 4500$ s, which corresponds to the time when the bottom proppant plug develops. Note that the kink on the pressure history at $t \approx 110$ s corresponds to reaching the stress barrier. There is no visible pressure change due to the injection of the proppant as well as due to the developing of the bottom plug.

To investigate the tip screen-out effect, Fig. 7 shows the results of a simulation for the reference parameter set, which includes leak-off. There are three features in the pressure diagram. First, there is a kink that corresponds to the time when the fracture reaches the stress barrier. Then, there is a characteristic pressure increase due to the development of the bottom proppant plug at $t \approx 1800$ s. After that, when the proppant reaches the top fracture tip, it causes an additional pressure rise at $t \approx 2000$ s. These observations are also supported by the length histories, which clearly indicate slower fracture growth due to the stress barriers, initiation of asymmetry at $t \approx 1800$ s, as well as slower propagation of the top fracture tip after the formation of a proppant plug there. Also note that the fracture width is noticeably affected by the formation of the proppant plugs.

4. Numerical solution for a P3D fracture

4.1. Problem formulation

To highlight the versatility of the proppant transport model, a simple multidimensional case is considered, namely the pseudo-3D (P3D) model for hydraulic fracture propagation with symmetrical stress barriers (Adachi et al., 2010). Fig. 8 shows the schematics of the fracture. The fracture is propagating between two symmetric stress barriers, where an additional stress $\Delta\sigma$ further compresses the fracture in the regions $|z| > H/2$. The fracture tip is assumed to be vertical, the horizontal length of the fracture is denoted by $l(t)$, while the height of the fracture is $h(x, t)$, see Fig. 8. Other assumptions of the model are: (i) the fluid pressure is uniform over the height of the fracture, i.e. does not depend on z , $p = p(x)$, which implies the symmetry of the fracture, (ii) a plain strain elasticity condition exists in any vertical (y, z) plane, and (iii)

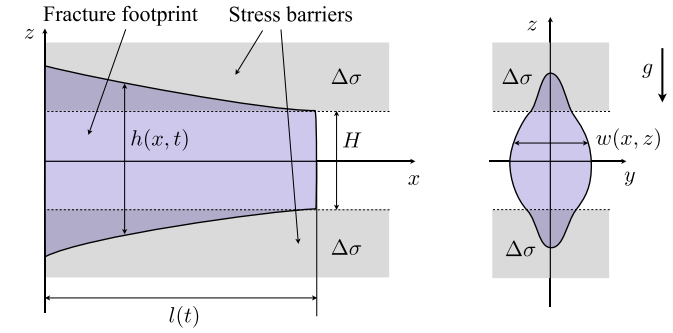


Fig. 8. Schematics of the P3D fracture.

leak-off occurs only in the reservoir layer ($|z| < H/2$) and follows the Carter's leak-off model (Carter, 1957).

To facilitate the development of the appropriate proppant transport model, it is useful to formulate the 2D equations for both fracture width and the particle concentration, so that

$$\begin{aligned} \frac{\partial w}{\partial t} + \frac{\partial q_x^s}{\partial x} + \frac{\partial q_z^s}{\partial z} + \frac{C' \mathcal{H}(H-2z) \mathcal{H}(2z+H)}{\sqrt{t-t_0(x)}} &= \frac{Q(z)}{H} \delta(x), \\ \frac{\partial w \bar{\phi}}{\partial t} + \frac{\partial q_x^p}{\partial x} + \frac{\partial q_z^p}{\partial z} &= \frac{\bar{\phi}_0 Q(z)}{H} \delta(x), \end{aligned} \quad (23)$$

where the fluxes are given in (2), $Q(z)$ is a source density that is distributed over the vertical coordinate z , and \mathcal{H} is a Heaviside step function. The boundary conditions for (23) require the vanishing of all fluxes along the fracture boundary, as well as the appropriate asymptotic behavior of the width near the vertical tips, see Peirce and Detournay (2008) for details. Following Adachi et al. (2010), since the pressure is assumed to be uniform over the height, the elasticity equations can be solved to obtain

$$\begin{aligned} w(x, z) &= \frac{2}{E'} (p(x) - \Delta\sigma) \chi \\ &+ \frac{4\Delta\sigma}{\pi E'} \left\{ \chi \arcsin\left(\frac{H}{h}\right) - z \ln \left| \frac{H\chi + 2z\psi}{H\chi - 2z\psi} \right| + \frac{H}{2} \ln \left| \frac{\chi + \psi}{\chi - \psi} \right| \right\}, \end{aligned} \quad (24)$$

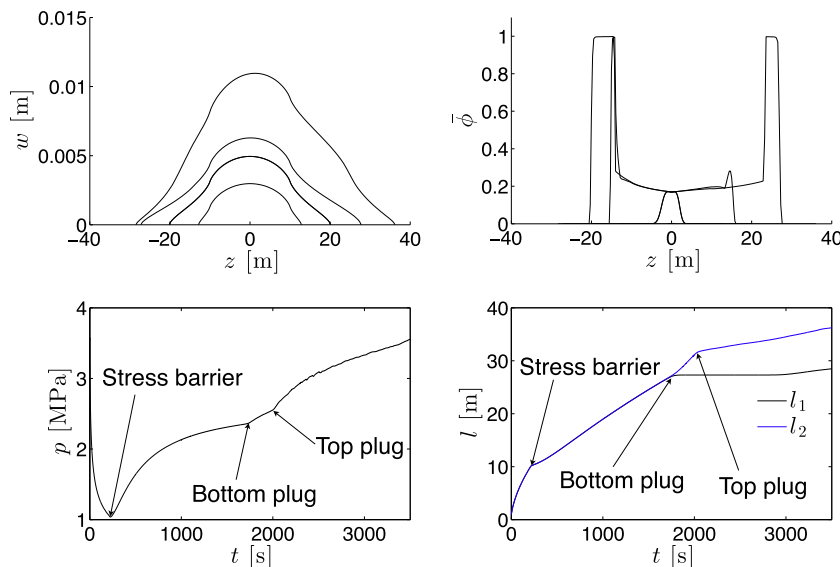


Fig. 7. The fracture width and proppant distribution (top pictures) for the reference parameter set and leak-off at different time instants $t_{ev} = 500$ s (no proppant at this time), 1100 s, 1800 s, and 3500 s. Bottom pictures show the histories of pressure at the inlet and the lengths l_1 (distance from the inlet to the bottom tip) and l_2 (distance from the inlet to the top tip).

where $\chi = \sqrt{h^2 - 4z^2}$, $\psi = \sqrt{h^2 - H^2}$, while E' as in (8) is the plane-strain Young's modulus. Again, as follows from Adachi et al. (2010), the application of the toughness propagation criterion leads to

$$p = \Delta\sigma \left[1 + \sqrt{\frac{2}{\pi H \Delta\sigma}} \sqrt{\frac{H}{h}} - \frac{2}{\pi} \arcsin\left(\frac{H}{h}\right) \right], \quad (25)$$

where K_{Ic} is mode I fracture toughness. Formulas (24) and (25) apply in the regions where $h > H$. When $h = H$, an elliptic fracture width profile is used instead of (24), i.e. $w = 2(E')^{-1} \chi p(x)$. To formulate the P3D model, one also needs to introduce average width, flux, and total inlet flux as follows:

$$\bar{w} = \frac{1}{H} \int_{-h/2}^{h/2} w dz, \quad \bar{q}_x^s = \frac{1}{H} \int_{-h/2}^{h/2} q_x^s dz, \quad Q_0 = \frac{1}{H} \int_{-h/2}^{h/2} Q(z) dz. \quad (26)$$

Note that $\bar{\phi}$ is an average concentration over the thickness (i.e. in the out-of-plane y direction) of the fracture, while \bar{w} and \bar{q}_x^s are respectively the width and flux, averaged over the height (i.e. z direction) of the fracture. With (26) in mind, Eq. (23a) can be integrated over z to obtain

$$\frac{\partial \bar{w}}{\partial t} + \frac{\partial \bar{q}_x^s}{\partial x} + \frac{C'}{\sqrt{t - t_0(x)}} = \frac{Q_0}{H} \delta(x), \quad (27)$$

where

$$\bar{q}_x^s = -\frac{\partial p}{\partial x} \frac{1}{H} \int_{-h/2}^{h/2} \left[\frac{w^3}{\mu'} Q^s(\bar{\phi}) + \frac{a^2 w}{\mu'} D(\bar{\phi}) \right] dz. \quad (28)$$

Relation (24) can also be integrated to obtain

$$\bar{w} = \frac{H}{E'} \left(\sqrt{\frac{\pi}{2H}} K_{Ic} \left(\frac{h}{H} \right)^{3/2} + \Delta\sigma \sqrt{\frac{h^2}{H^2} - 1} \right), \quad h > H, \quad (29)$$

Given the fact that p can be expressed as a function of \bar{w} from (25) and (29), Eq. (27) can be solved if the variation of $\bar{\phi}$ versus z is provided (so that the integral in (28) can be calculated). Once solved for \bar{w} , (29) can be used to find h , which finally allows us to obtain w from (24) and (25). In other words, knowing the average width \bar{w} is enough to “restore” the fracture width profile w . This property allows us to obtain the 2D fracture footprint by solving the one-dimensional problem governed by (27). Unfortunately, such a useful “restoring” property does not apply for the proppant. Indeed, having only the average proppant concentration is not sufficient to “restore” the concentration profile, as there are many different (physically admissible) particle distributions that can have the same mean value. For this reason, a 2D proppant transport model has to be considered.

To assist the solution of the proppant transport equation, the vertical (or z) component of the slurry flux has to be computed first. Formally, due to the assumptions of the model, there is no pressure gradient in the vertical direction, which implies no flux in the vertical direction. This, however, should be interpreted in a sense that the vertical flux is small compared to the horizontal flux, but not necessary zero. To find the vertical component of the slurry flux, one can integrate (23a) to determine

$$q_z^s = \int_{-h/2}^z \left[\frac{Q(z)}{H} \delta(x) - \frac{C' \mathcal{H}(H - 2z) \mathcal{H}(2z + H)}{\sqrt{t - t_0(x)}} - \frac{\partial w}{\partial t} - \frac{\partial q_x^s}{\partial x} \right] dz. \quad (30)$$

Finally, the system of equations that describes the P3D problem with proppant is

$$\begin{aligned} \frac{\partial \bar{w}}{\partial t} + \frac{\partial \bar{q}_x^s}{\partial x} + \frac{C'}{\sqrt{t - t_0(x)}} &= \frac{Q_0}{H} \delta(x), \\ \frac{\partial w \bar{\phi}}{\partial t} + \frac{\partial q_x^p}{\partial x} + \frac{\partial q_z^p}{\partial z} &= \frac{\bar{\phi}_0 Q(z)}{H} \delta(x), \end{aligned} \quad (31)$$

where \bar{q}_x^s is given in (28), the relations between w , \bar{w} , p , and h are given by (24), (25) and (29), while the proppant fluxes are

$$\begin{aligned} q_x^p &= -B \left(\frac{w}{a} \right) \frac{w^3}{\mu'} \frac{\partial p}{\partial x} Q^p(\bar{\phi}), \\ q_z^p &= B \left(\frac{w}{a} \right) \hat{Q}^p \left(\bar{\phi}, \frac{w}{a} \right) q_z^s - B \left(\frac{w}{a} \right) \frac{a^2 w}{\mu'} (\rho^p - \rho^f) g \hat{G}^p \left(\bar{\phi}, \frac{w}{a} \right), \end{aligned} \quad (32)$$

where g is the gravitational acceleration constant. The boundary conditions for (31) are

$$\bar{q}_x^s|_{x=l} = 0, \quad \bar{w}|_{x=l} = 0. \quad (33)$$

Note that the boundary conditions at the top and bottom sides of the fracture are accounted for in (30). Also, the blocking function B restricts the presence of the particles near the fracture tip, so that the zero-proppant-flux boundary condition is always satisfied automatically.

4.2. Numerical algorithm

To facilitate the numerical calculations, first, the problem parameters are scaled as

$$\begin{aligned} \hat{l} &= \frac{l}{l_*}, \quad \hat{h} = \frac{h}{h_*}, \quad \hat{t} = \frac{t}{t_*}, \quad \hat{w} = \frac{w}{w_*}, \quad \hat{p} = \frac{p}{p_*}, \quad \hat{q}_x^s = \frac{q_x^s}{q_*}, \quad \hat{q}_z^s = \frac{l_* q_z^s}{h_* q_*}, \\ \hat{K} &= \frac{K_{Ic}}{K_*}, \quad \hat{C} = \frac{C'}{C_*}, \quad \hat{a} = \frac{a}{a_*}, \quad \hat{g} = \frac{g}{g_*}, \end{aligned} \quad (34)$$

where all “hat” quantities are dimensionless, while the scaling factors are computed as

$$\begin{aligned} l_* &= \frac{H^4 \Delta\sigma^4}{Q_0 \mu' E'^3}, \quad h_* = H, \quad t_* = \frac{\Delta\sigma^5 H^6}{Q_0^2 \mu' E'^4}, \quad w_* = \frac{H \Delta\sigma}{E'}, \quad p_* = \Delta\sigma, \quad q_* = \frac{Q_0}{H}, \\ K_* &= \Delta\sigma \sqrt{\frac{2H}{\pi}}, \quad C_* = \frac{Q_0 E' \mu'^{1/2}}{H^2 \Delta\sigma^{3/2}}, \quad a_* = \frac{H \Delta\sigma}{E'}, \quad g_* = \frac{Q_0^2 \mu'^2 E'^6}{\Delta\rho H^7 \Delta\sigma^7}. \end{aligned} \quad (35)$$

The biggest advantage of this scaling lies in the fact that it highlights the number of independent parameters that govern the problem. For this problem, there are four of such quantities: \hat{K} , \hat{C} , \hat{a} and \hat{g} . Note that the scaling (34) is done slightly differently from Adachi et al. (2010).

To aid the solution of the moving boundary problem, a moving mesh in both x and z directions is introduced. The following scaled coordinates are introduced as

$$\xi = \frac{x}{\hat{l}}, \quad \zeta = \frac{z}{\hat{h}}, \quad (36)$$

where $\hat{l} = \hat{l}(\hat{t})$ and $\hat{h} = \hat{h}(\hat{\zeta}, \hat{t})$. In this case, the derivatives transform as

$$\begin{aligned} \frac{\partial(\cdot)}{\partial t} \Big|_{x,z} &= \frac{\partial(\cdot)}{\partial \hat{t}} \Big|_{\xi,\zeta} - \frac{V \xi \partial(\cdot)}{\hat{l} \partial \xi} \Big|_{\xi,\zeta} - \left(\frac{\partial \hat{h}}{\partial \hat{t}} - \frac{V \zeta \partial \hat{h}}{\hat{l} \partial \xi} \right) \frac{\zeta \partial(\cdot)}{\hat{h} \partial \zeta} \Big|_{\xi,\zeta}, \\ \frac{\partial(\cdot)}{\partial x} \Big|_{t,z} &= \frac{1}{\hat{l}} \frac{\partial(\cdot)}{\partial \xi} \Big|_{\xi,\zeta} - \frac{\partial \hat{h}}{\partial \xi} \frac{\zeta \partial(\cdot)}{\hat{h} \partial \zeta} \Big|_{\xi,\zeta}, \\ \frac{\partial(\cdot)}{\partial z} \Big|_{t,x} &= \frac{1}{\hat{h}} \frac{\partial(\cdot)}{\partial \zeta} \Big|_{\xi,\zeta}, \end{aligned} \quad (37)$$

where $V = d\hat{l}/d\hat{t}$ is the velocity of the crack tip. By substituting (37) into (31), and simplifying the result, one may write

$$\frac{\partial \hat{w}}{\partial \hat{t}} - \frac{V\xi}{\hat{l}} \frac{\partial \hat{w}}{\partial \xi} + \frac{1}{\hat{l}} \frac{\partial \hat{q}_x^s}{\partial \xi} + \frac{\hat{C}}{\sqrt{\hat{t} - t_0(\hat{l}\xi)}} = \frac{1}{\hat{l}} \delta(\xi),$$

$$\frac{\partial \hat{h}\hat{l}\hat{w}\hat{\phi}}{\partial \hat{t}} + \frac{\partial \hat{q}_x^p}{\partial \xi} + \frac{\partial \hat{q}_z^p}{\partial \xi} = \hat{\phi}_0 \hat{h} \hat{Q}(\xi) \delta(\xi),$$

where

$$\hat{q}_x^p = \hat{h}(\hat{q}_x^p - V\xi\hat{w}\hat{\phi}), \quad \hat{q}_z^p = \hat{l}\hat{q}_z^p - \frac{\partial \hat{h}}{\partial \hat{t}} \hat{l}\xi\hat{w}\hat{\phi} - \frac{\partial \hat{h}}{\partial \xi} \zeta \frac{\hat{q}_x^p}{\hat{h}},$$

are the fluxes that account for the moving mesh terms. Note that similar changes of variables can be applied to (23a), in which case the integral (30) for the calculation of the flux transforms to

$$\hat{q}_z^s = \left(\frac{\partial \hat{h}}{\partial \hat{t}} \hat{w} + \frac{\partial \hat{h}}{\partial \xi} \frac{\hat{q}_x^s}{\hat{h}\hat{l}} \right) \zeta + \frac{1}{\hat{l}} \times \int_{-1/2}^{\xi} \left[\hat{h}\hat{Q}(\zeta)\delta(\zeta) - \hat{h}\hat{C}\mathcal{H}(1-2\hat{h}\zeta)\mathcal{H}(2\hat{h}\zeta+1) - \frac{\partial \hat{h}\hat{l}\hat{w}}{\partial \hat{t}} - \frac{\partial \hat{q}_x^s}{\partial \xi} \right] d\zeta,$$

where

$$\hat{q}_x^s = \hat{h}(\hat{q}_x^s - V\xi\hat{w}).$$

Note that the fluxes in (39) can also be derived from physical considerations. Fig. 9 shows the elements in the physical (on the left) and computational (on the right) domains. The fluxes in the picture are generic and can be applied to either the slurry or proppant. The element in the computational domain is rectangular and does not move, while the corresponding element in the physical domain is distorted and moves horizontally with velocity $V\xi$ and vertically with velocity $\partial\hat{h}/\partial\hat{t}\zeta$. The angle θ can be found from $\tan(\theta) = -\partial\hat{h}/\partial\xi\zeta/\hat{l}$. Since the fluxes through the sides of the element should be preserved, one can write

$$\left(\hat{q}_x^p - V\xi\hat{w}\hat{\phi} \right) \hat{h}\Delta\zeta = \hat{q}_x^p \Delta\zeta,$$

$$\left(\hat{q}_z^p - \frac{\partial \hat{h}}{\partial \hat{t}} \zeta \hat{w}\hat{\phi} + \left(\hat{q}_x^p - V\xi\hat{w}\hat{\phi} \right) \tan(\theta) \right) \hat{l}\Delta\xi = \hat{q}_z^p \Delta\xi,$$

which allows us to recover (39).

To close the system of equations, it is noted that

$$\hat{q}_x^s = -\frac{1}{\hat{l}} \frac{\partial \hat{p}}{\partial \xi} \left[\hat{w}^3 Q^s(\bar{\phi}) + \hat{a}^2 \hat{w} D(\bar{\phi}) \right],$$

$$\hat{q}_z^s = -\frac{\hat{h}}{\hat{l}} \frac{\partial \hat{p}}{\partial \xi} \int_{-1/2}^{1/2} \left[\hat{w}^3 Q^s(\bar{\phi}) + \hat{a}^2 \hat{w} D(\bar{\phi}) \right] d\zeta,$$

$$\hat{q}_x^p = B\left(\frac{\hat{w}}{\hat{a}}\right) \hat{Q}^p\left(\bar{\phi}, \frac{\hat{w}}{\hat{a}}\right) \hat{q}_x^s,$$

$$\hat{q}_z^p = B\left(\frac{\hat{w}}{\hat{a}}\right) \hat{Q}^p\left(\bar{\phi}, \frac{\hat{w}}{\hat{a}}\right) \hat{q}_z^s - B\left(\frac{\hat{w}}{\hat{a}}\right) \hat{a}^2 \hat{w} \hat{g} \hat{G}^p(\bar{\phi}),$$

where the pressure derivative is

$$\frac{\partial \hat{p}}{\partial \xi} = \frac{d\hat{p}}{d\hat{h}} \frac{d\hat{h}}{d\hat{w}} \frac{d\hat{w}}{d\xi} = Y(\hat{h}) \frac{d\hat{w}}{d\xi},$$

where

$$Y(\hat{h}) = \frac{d\hat{p}}{d\hat{h}} \frac{d\hat{h}}{d\hat{w}} = \frac{4\sqrt{\hat{h} - 2\hat{K}\sqrt{\hat{h}^2 - 1}}}{\pi\hat{h}^2(3\hat{K}\sqrt{\hat{h}^2 - 1} + 2\sqrt{\hat{h}})}.$$

Finally, to “restore” the fracture opening based on the average width, one can rewrite (24), (25) and (29) as

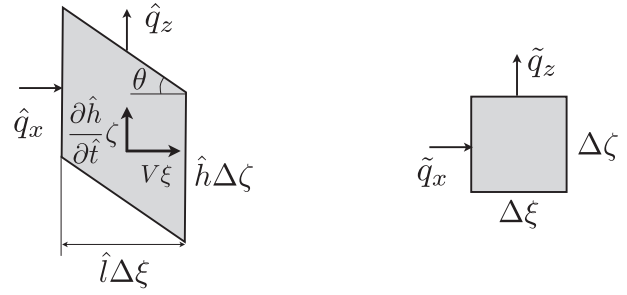


Fig. 9. The element in the physical domain (left) and the computational domain (right).

$$\hat{w}(\hat{h}) = \frac{4}{\pi} \left[\hat{K}\hat{\chi}\sqrt{\hat{h}} - \hat{h}\zeta \ln \left| \frac{\hat{\chi} + 2\zeta\hat{\psi}}{\hat{\chi} - 2\zeta\hat{\psi}} \right| + \frac{1}{2} \ln \left| \frac{\hat{h}\hat{\chi} + \hat{\psi}}{\hat{h}\hat{\chi} - \hat{\psi}} \right| \right],$$

$$\hat{w}(\hat{h}) = \hat{K}\hat{h}^{3/2} + \sqrt{\hat{h}^2 - 1}, \quad \hat{h} > 1,$$

where $\hat{\chi} = \sqrt{1 - 4\zeta^2}$ and $\hat{\psi} = \sqrt{\hat{h}^2 - 1}$. Relations (44) allow us to calculate a function $\hat{w}(\hat{w})$, i.e. “restore” the fracture width. When $\hat{h} = 1$, the latter equations combine to yield

$$\hat{w} = \frac{4}{\pi} \sqrt{1 - 4\zeta^2 \hat{w}}, \quad \hat{h} = 1.$$

The numerical algorithm for the P3D geometry is somewhat similar to that for the KGD fracture, in that it is divided into two main parts: (i) calculating the fracture propagation and (ii) updating the proppant concentration inside the fracture. Since the equation for the fracture propagation is very similar to that for the KGD fracture, a similar algorithm is used to update the fracture footprint. The average width \hat{w} is approximated by a piece-wise constant function, the time derivative is approximated by backward differences, and the integral in (41) is approximated using the midpoint rule, in which case (38a) is reduced to a system of algebraic equations that is solved iteratively. The big difference, however, lies in the absence of a pressure singularity near the right tip, in which case the velocity of the crack tip is calculated based on a zero flux condition. Eq. (38b) is solved numerically using a finite volume method and a generalization of the one-dimensional algorithm shown in Fig. 5. The analog of the condition (20) is

$$\hat{q}_x^s = \text{const.},$$

i.e. the average flux stays constant during the differentiation with respect to $\bar{\phi}$. Another difference comes from the fact, that a line source has to be used, and, moreover, that the line cannot go all the way to the fracture boundary since the proppant cannot be there due to the blocking function. The distribution of the intensity of the source is taken proportional to the cube of the fracture width, and contained inside $w > (2N + \frac{1}{2})a$ ($N = 3$ is used for all calculations). In this case there is no proppant in the prohibited areas and the source is concentrated near the centre of the fracture height. Other details about the numerical scheme are analogous to the 1D model and omitted for brevity.

4.3. Numerical examples

This section covers several numerical examples that highlight the effects associated with the presence of proppant. First, it should be noted that the numerical code (without proppant) was tested against the solutions in Adachi et al. (2010), and the results showed good agreement. There are two main effects associated with the presence of the proppant, that are considered in the examples: (i) gravitational settling and (ii) tip screen-out.

All figures in this section that plot the fracture footprint and show the proppant concentration in color. Note that the maximum value for $\bar{\phi}$ is 1, since the concentration is scaled by ϕ_m . For all figures, simulations start at $t_{\text{start}} = 1$ s, with $l = 1$ m, and an elliptical width profile with a maximum opening $w_{\text{max}} = 10^{-3}$ m. At time t_{pr} the proppant is introduced, and at t_{end} the simulation stops. Note that the effect of the initial condition decays with time, so, as long as the total initial volume of the fracture is sufficiently small, there is practically no effect associated with the initial condition. The reference problem parameters are $H = 25$ m for the width of the reservoir layer, $\mu' = 1.2$ Pa s for the shear viscosity (times 12), $E' = 25 \times 10^9$ Pa for the plane strain modulus, $Q_0 = 2 \times 10^{-2}$ m³/s for the injection rate, $\Delta\sigma = 2.5 \times 10^6$ Pa for the magnitude of the stress barriers, $\Delta\rho = 800$ kg/m³ for the difference between proppant and carrying fluid mass densities, $K_{1c} = 10^6$ Pa m^{1/2} for the fracture toughness, $C' = 5 \times 10^{-5}$ m/s^{1/2} for the leak-off coefficient, $a = 4 \times 10^{-4}$ m for the particle radius, $g = 9.8$ m/s² for the gravity constant, $\bar{\phi}_0 = 0.2$ for the proppant concentration at the inlet, and $t_{\text{pr}} = 1000$ s for the start time of proppant injection. At the same time, different values of t_{end} are used. For all the figures in this section, the parameters are assumed to be taken from the above reference set, except those, which are specified directly.

It is important to recognize the presence of the time scale associated with the gravitational settling. The asymptotic behavior of the function $\hat{C}^p(\bar{\phi})$ (see Dontsov and Peirce, 2014) can be used to estimate the settling velocity, while the settling time can be calculated based on the vertical distance the proppant needs to travel, which is 1/2 in the scaled formulation. Combining these assumptions and the last equation in (41), the settling time can be estimated as

$$t_s = \frac{t_*}{2\hat{v}_{\text{settl}}} = \frac{1}{2\frac{8}{3}\hat{a}^2\hat{g}}t_* = \frac{3H\mu'}{16\Delta\rho ga^2},$$

where \hat{v}_{settl} is the dimensionless settling velocity calculated for small particle concentrations. This settling time needs to be compared to the proppant injection duration. Since the proppant is first injected at t_{pr} , the duration of the injection is $t_{\text{end}} - t_{\text{pr}}$. In this case, it might be useful to introduce the ratio between two time scales which determines whether the gravitational settling is significant or not

$$G_s = \frac{16\Delta\rho ga^2(t_{\text{end}} - t_{\text{pr}})}{3H\mu'}. \quad (45)$$

If the parameter $G_s \gg 1$, then the settling occurs before the end of the fracturing job, while if $G_s \ll 1$, then the gravity does not affect the proppant distribution much. ~~It is interesting to note that if $t_{\text{end}} - t_{\text{pr}} = \text{const}$, the viscosity does not enter (45), so that changing the viscosity of the carrier fluid alone cannot be used to alter the settling pattern. This counterintuitive phenomenon can be understood in the following way: a higher viscosity leads to a slower vertical settling velocity, however, at the same time, the horizontal velocity becomes smaller too. Since both settling and horizontal velocities are proportional to the inverse of the viscosity, the direction of the velocity vector does not change, and so the proppant pattern is unaffected. However, if the design fracture length is regarded as fixed, then the total treatment time t_{end} becomes a function of viscosity, and then G_s will no longer be independent of μ' . In addition, since high powers of E' , $\Delta\sigma$ and H appear in the scaling parameters (34), and in particular in (45), the fracture footprint and proppant distribution become very sensitive to the values of~~

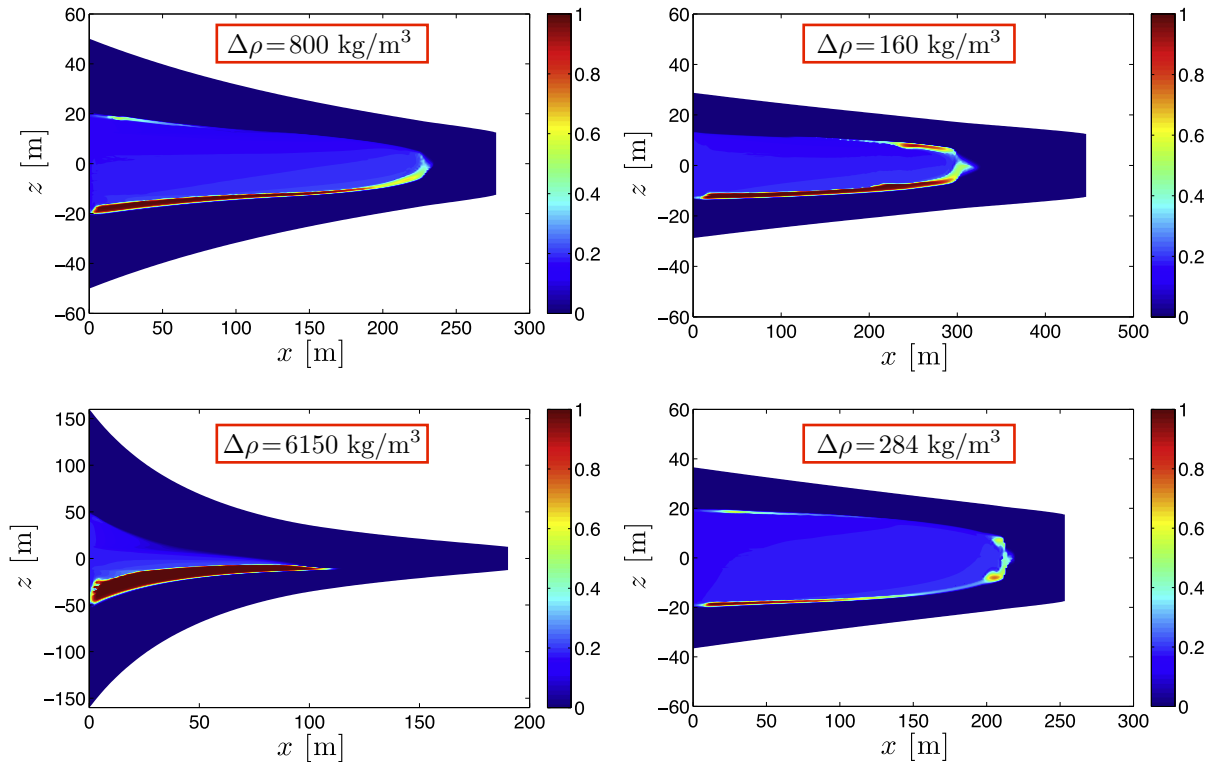


Fig. 10. Fracture footprint and the proppant concentration $\bar{\phi}$ indicated by color calculated for the reference parameters and $t_{\text{end}} = 4000$ s, except $C' = 0$ (top left), $C' = 0$ and $\mu' = 0.24$ Pa s (top right), $C' = 0$ and $\Delta\sigma = 1.5 \times 10^6$ Pa (bottom left) and $C' = 0$ and $H = 35$ m (bottom right). The gravitational settling parameters are $G_s = 0.67$ for both top pictures (notable settling), $G_s = 5.15$ for the bottom left picture (significant settling), and $G_s = 0.17$ for the bottom right picture (almost no settling).

~~E' , $\Delta\sigma$ and H . In other words, if any of those quantities is measured inaccurately, the prediction of the model can be unreliable.~~

To illustrate the importance of the parameter G_s , Fig. 10 plots the distribution of $\bar{\phi}$ for different values of G_s . As can be seen from Fig. 10, $G_s = O(1)$ leads to some skewness of the proppant distribution, which is nearly identical (as it should be) for the top pictures. The bottom left picture corresponds to $G_s \gg 1$, and so the effect of the gravity is significant. The bottom right picture corresponds to $G_s \ll 1$, and so the effect of the gravitational settling is minimal. One can also see the effect of the “blocking” functions, as the proppant cannot sink all the way to the bottom of the fracture and the maximum concentration in the plug does not increase beyond unity (the maximum allowed concentration).

Crack tip screen-out is another very important consequence of the presence of proppant. It is important to recognize that particles can reach the crack tip even without leak-off. First, the proppant flows faster by a factor 1.2 for small concentrations, which can be concluded from the asymptotic behavior of \hat{Q}^p , see Dontsov and Peirce (2014). This happens because of the nonuniform distribution of particles over the width of the channel. A similar thing happens in the vertical direction, the proppant tends to flow in the areas where the fracture is wide, while the fluid flows everywhere inside the fracture. So, the proppant gets concentrated near the centre, which again implies that, on average, it flows faster than

the slurry. To illustrate this phenomenon, Fig. 11 plots the fracture footprints and the proppant distributions at different time instants $t = 800$ s, $t = 1200$ s, $t = 3000$ s and $t = 4500$ s for $C' = 0$ (other parameters are taken from the reference set). The variation of the pressure at the inlet, the length of the fracture, and the height at the inlet versus time are also shown. As can be seen from the pictures, the length of the fracture is below 100 m right before the proppant injection starts, and by a length of 300 m, the proppant is already in the tip region. The proppant travels approximately 250 m, while the fracture grows by 200 m during the same time period, which shows that the proppant is faster by approximately 25%. There is no plug formation (in the x direction), however, at these times and the proppant is distributed almost uniformly inside the fracture. At the same time, there is a plug in the vertical z direction due to gravitational settling. The variation of the pressure, the length, and the height is smooth, although there is a small kink at $t = 1000$, which corresponds to the beginning of proppant input.

To promote the accumulation of proppant in the tip region, leak-off needs to be introduced. Fig. 12 plots the fracture footprint and the proppant distribution at different time instants $t = 800$ s, $t = 1200$ s, $t = 1700$ s and $t = 3000$ s (all parameters are taken from the reference set). The variation of the pressure at the inlet, the length of the fracture, and the height at the inlet versus time

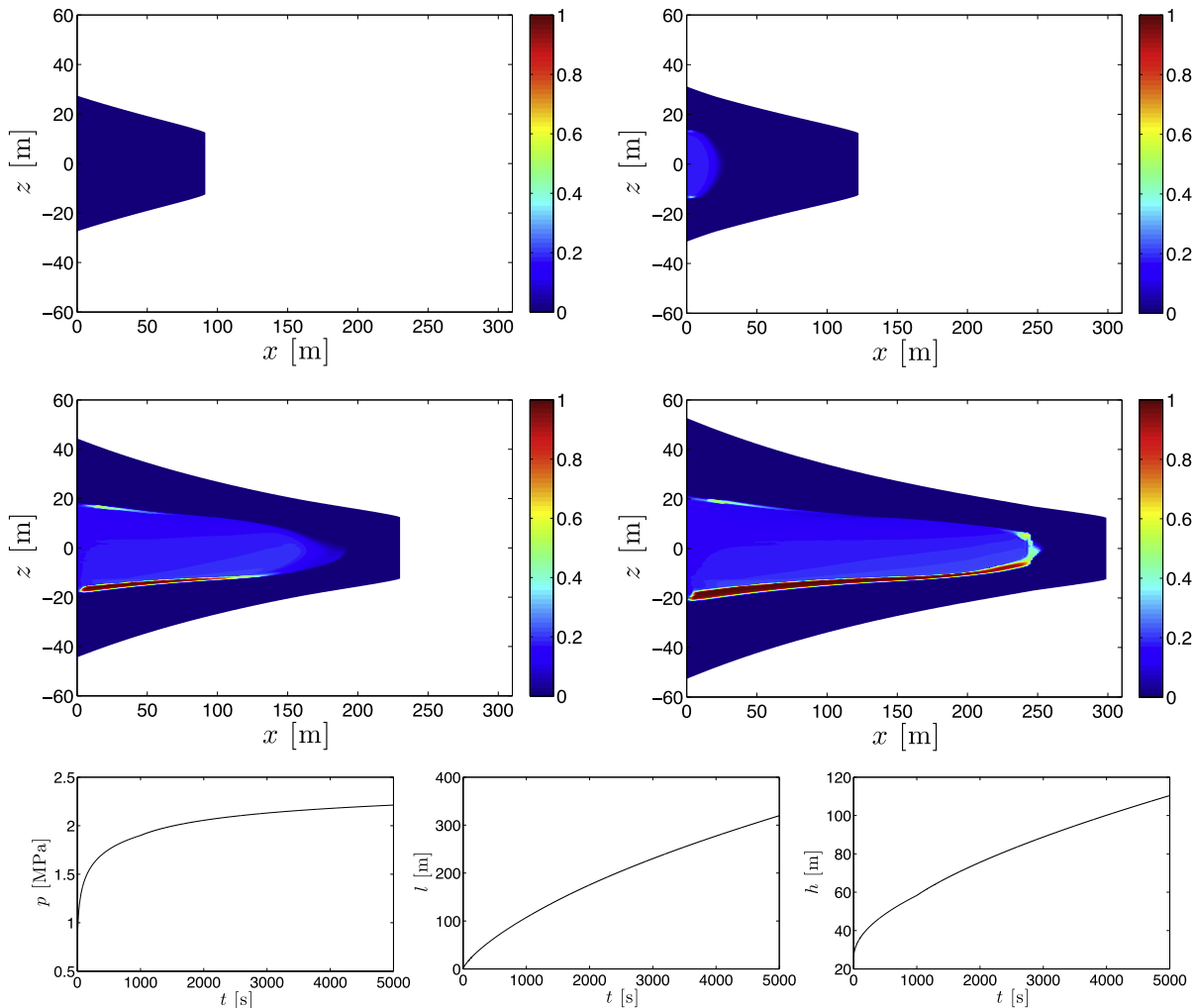


Fig. 11. Fracture footprint with the proppant concentration $\bar{\phi}$ indicated by color calculated for the reference parameters and $C' = 0$ at $t = 800$ s (top left), $t = 1200$ s (top right), $t = 3000$ s (centre left) and $t = 4500$ s (centre right). The case with $t = 4500$ s corresponds to $G_s = 0.89$. Bottom pictures show the pressure at the inlet, the length of the fracture, and the height of the fracture at the inlet versus time.

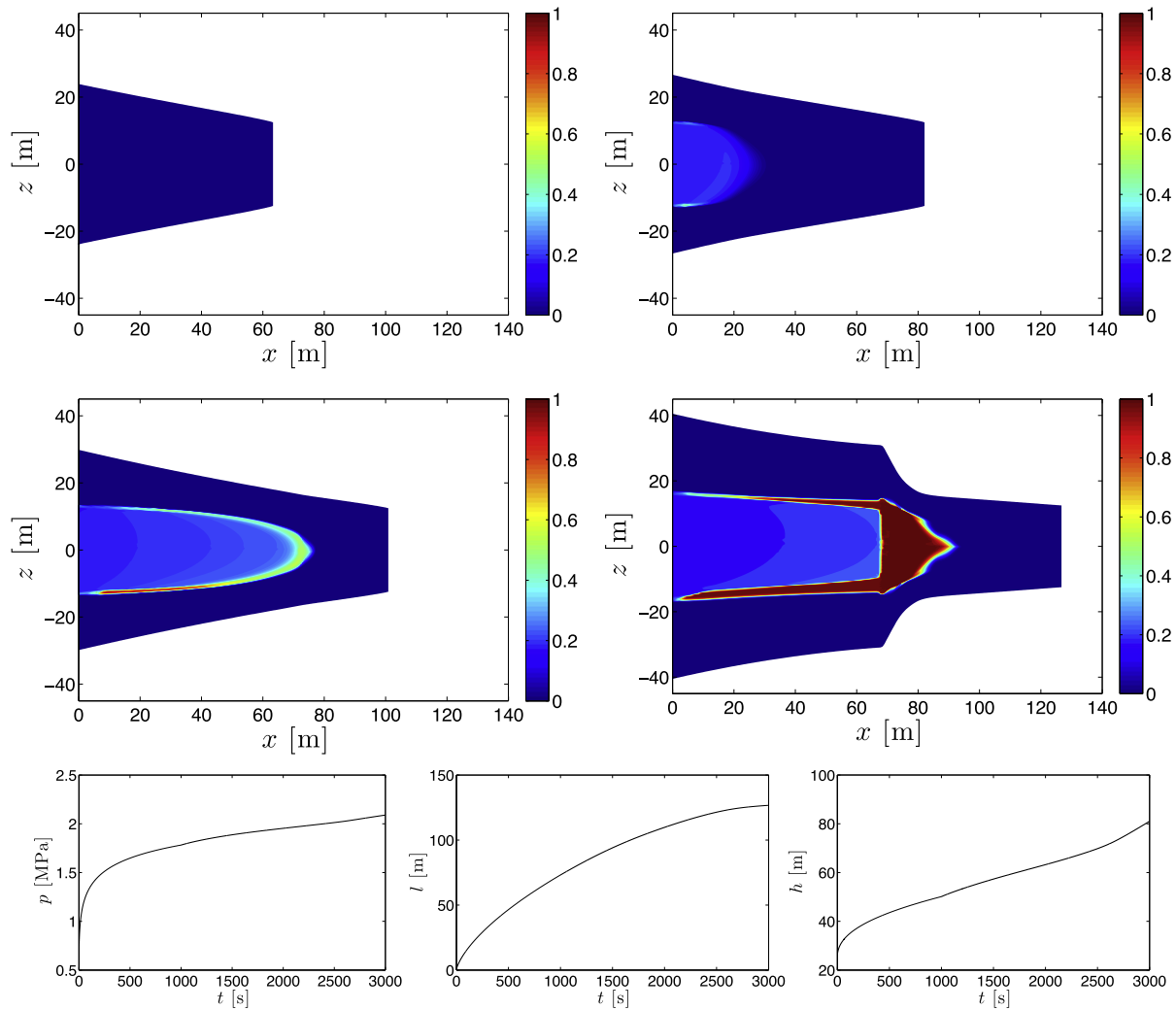


Fig. 12. Fracture footprint with the proppant concentration $\bar{\phi}$ indicated by color calculated for the reference parameters at $t = 800$ s (top left), $t = 1200$ s (top right), $t = 1700$ s (centre left) and $t = 3000$ s (centre right). The case with $t = 3000$ s corresponds to $G_s = 0.45$. Bottom pictures show the pressure at the inlet, the length of the fracture, and the height of the fracture at the inlet versus time.

are also shown. As can be seen, the leak-off significantly retards the fracture propagation, and even at $t = 800$, the fracture is 50% shorter compared to that in Fig. 11. Once the proppant is introduced, it reaches the crack tip much faster, accumulates there, and significantly slows further fracture propagation. After the plug is formed, only a small amount of fluid can penetrate and so the fracture starts to grow noticeably in the vertical direction.

5. Summary

This paper applies a model for proppant transport, which is based on an empirical constitutive law for the mixture of a viscous fluid with spherical particles, to two hydraulic fracturing problems, namely with the KGD and the P3D geometries. In the adopted formulation, the slurry flux has two terms, one Poiseuille-law-type term with an effective viscosity (which goes to infinity as the concentration reaches a critical value), and a Darcy-law-type term, where the average velocity is proportional to the particle size squared and the pressure gradient. The flux of the particles also has two terms, one proportional to the slurry flux, and another related to gravitational forces. The first term describes the advective motion, while the second term describes gravitational settling. The proppant transport model is first applied to the KGD fracture

geometry with stress barriers. The numerical simulations show that the developed model is able to capture the initiation and further growth of a proppant plug in the crack tip region, which leads to tip screen-out. The gravitational settling introduces asymmetry, leads to faster screen-out on one side of the crack, and may stop the propagation there for some time. The proppant transport model is then implemented with the P3D fracture geometry. Despite the fact that the P3D model reduces to the solution of a 1D equation, the proppant transport cannot be treated in a similar fashion, and requires the numerical solution of a 2D problem. Two main objectives in the analysis of the numerical solutions include the gravitational settling and tip screen-out. A dimensionless parameter, which controls the magnitude of the particle settling, is introduced. ~~One interesting fact is that this parameter does not directly depend on the viscosity of the fluid.~~ It is further shown that the particles can reach the tip of the fracture even without leak-off. This occurs due to the fact that the proppant is concentrated near the centre of the channel, and thus, on average, gets transported faster than the carrying fluid. When leak-off is introduced, the proppant reaches the crack tip region notably faster and accumulates there forming a plug. Once the plug is developed, only a small amount of fluid can penetrate the plug (due to the Darcy-law-type term), which switches fracture growth predominantly to the vertical direction. The main drawbacks of the model include: its

inability to capture asymmetry caused by gravitational settling; and the rigid plug property, in which the proppant can sustain some stress once the fracture tends to close. Both issues cannot be implemented since one of the key assumptions of the P3D model – uniform pressure over the height of the fracture (and the resulting solution of the elasticity equation), would not be satisfied. This could be overcome only by adding a proppant transport module into a fully planar 3D hydraulic fracture propagation model, which is a challenging problem for future research.

Acknowledgments

The authors gratefully acknowledge the support of the British Columbia Oil and Gas Commission and the NSERC of Canada discovery grants program.

References

- Frank, U., Barkley, N., 2005. Remediation of low permeability subsurface formations by fracturing enhancements of soil vapor extraction. *J. Hazard. Mater.* 40, 191–201.
- Abou-Sayed, A., Andrews, D., Buhidma, I., 1989. Evaluation of oily waste injection below the permafrost in prudhoe bay field. In: *Proceedings of the California Regional Meetings*, Bakersfield, CA, Society of Petroleum Engineers, Richardson, TX, pp. 129–142.
- Jeffrey, R., Mills, K., 2000. Hydraulic fracturing applied to inducing longwall coal mine goaf falls. In: *Pacific Rocks 2000*, Balkema, Rotterdam, pp. 423–430.
- Economides, M., Nolte, K. (Eds.), 2000. *Reservoir Stimulation*, 3rd Edition. John Wiley & Sons, Chichester, UK.
- Khristianovic, S., Zheltov, Y., 1955. Formation of vertical fractures by means of highly viscous fluids. In: *Proc. 4th World Petroleum Congress*, vol. 2, pp. 579–586.
- Garagash, D., Detournay, E., 2000. Near tip processes of a fluid-driven fracture. *ASME J. Appl. Mech.* 67, 183–192.
- Adachi, J., Detournay, E., 2002. Self-similar solution of a plane-strain fracture driven by a power-law fluid. *Int. J. Numer. Anal. Methods Geomech.* 26, 579–604.
- Detournay, E., Garagash, D., 2003. The tip region of a fluid-driven fracture in a permeable elastic solid. *J. Fluid. Mech.* 494, 1–32.
- Detournay, E., 2004. Propagation regimes of fluid-driven fractures in impermeable rocks. *Int. J. Geomech.* 4, 1–11.
- Adachi, J., Siebrits, E., Peirce, A., Desroches, J., 2007. Computer simulation of hydraulic fractures. *Int. J. Rock Mech. Min. Sci.* 44, 739–757.
- Peirce, A., Detournay, E., 2008. An implicit level set method for modeling hydraulically driven fractures. *Comput. Methods Appl. Mech. Eng.* 197, 2858–2885.
- Dontsov, E., Peirce, A., 2014. Slurry flow, gravitational settling, and a proppant transport model for hydraulic fractures. *J. Fluid Mech.* 760, 567–590.
- Boyer, F., Guazzelli, E., Pouliquen, O., 2011. Unifying suspension and granular rheology. *Phys. Rev. Lett.* 107, 188301.
- Boronin, S., Osiptsov, A., 2010. Two-continua model of suspension flow in a hydraulic fracture. *Dokl. Phys.* 55, 199–202.
- Chekhonin, E., Levonyan, K., 2012. Hydraulic fracture propagation in highly permeable formations, with applications to tip screenout. *Int. J. Rock Mech. Min.* 50, 19–28.
- Eskin, D., Miller, M., 2008. A model of non-newtonian slurry flow in a fracture. *Powder Technol.* 182, 313–322.
- Lister, J., 1990. Buoyancy-driven fluid fracture: the effects of material toughness and of low-viscosity precursors. *J. Fluid. Mech.* 210, 263–280.
- Carter, E., 1957. Optimum fluid characteristics for fracture extension. In: Howard, G.C., Fast, C.R. (Eds.), *Drilling and Production Practices*, pp. 261–270.
- Adachi, J., 2001. Fluid-driven fracture in permeable rock (Ph.D. thesis). University of Minnesota.
- Bale, D., LeVeque, R.J., Mitran, S., Rossmanith, J.A., 2002. A wave-propagation method for conservation laws and balance laws with spatially varying flux functions. *SIAM J. Sci. Comput.* 24, 955–978.
- LeVeque, R., 2002. *Finite Volume Methods for Hyperbolic Problems*. Cambridge University Press.
- Adachi, J.I., Detournay, E., Peirce, A.P., 2010. An analysis of classical pseudo-3D model for hydraulic fracture with equilibrium height growth across stress barriers. *Int. J. Rock Mech. Min. Sci.* 47, 625–639.